

# Controlled Manipulation of Small- and Large- Scales in a Turbulent Shear Layer, Part I: Experimental Studies

Bojan Vukasinovic<sup>\*</sup>, Davidson G. Lucas<sup>†</sup>, and Ari Glezer<sup>‡</sup>  
 Woodruff School of Mechanical Engineering,  
 Georgia Institute of Technology, Atlanta, GA 30332-0405

The effects of fluidic actuation of small- and large-scale structures in a single stream, plane shear layer are investigated experimentally. While small-scale motions are effected by direct, high-frequency actuation (compared to the “natural” frequency of the baseline flow), large-scale coherent motions (at scales comparable to the cross stream width of the layer) are induced *indirectly* by transients associated with onset and termination of the actuation. High-resolution PIV and hot wire measurements show that large vortical structures are formed by rollup that follows the transient disruption of vorticity flux in the upstream boundary layer. The high-frequency actuation couples to the shear layer via the formation of a train of vortices at the actuation frequency that are advected along the high-speed edge of the layer. Concomitant excitation of *both* small and large scales leads to enhanced mixing through direct enhancement of the small-scale motions and augmented entrainment by the induced large-scales. As a result, the turbulent kinetic energy (especially within the large scales) as well as the cross stream spreading of the layer are significantly enhanced. In the absence of the transients that lead to the formation of the large scale structures, continuous high-frequency actuation results in enhanced dissipation and thereby stabilization of the base flow.

## Nomenclature

|                  |   |  |
|------------------|---|--|
| $\theta$         | = | boundary layer momentum thickness          |
| $\rho$           | = | fluid density                              |
| $\phi$           | = | phase angle                                |
| $b$              | = | shear layer width                          |
| $b_j$            | = | actuator orifice width                     |
| $C_\mu$          | = | actuator jet momentum coefficient          |
| $f_{AM}$         | = | amplitude-modulation frequency             |
| $f_c$            | = | crossover frequency                        |
| $H$              | = | step height                                |
| $k$              | = | turbulent kinetic energy                   |
| $U_i$            | = | $i$ -component of the velocity             |
| $\overline{U}_i$ | = | $i$ -component of the mean velocity        |
| $u_i$            | = | fluctuating $i$ -component of the velocity |
| $U_0$            | = | free stream velocity                       |
| $U_j$            | = | average jet velocity                       |
| $Re$             | = | Reynolds number                            |
| $St$             | = | Strouhal number                            |

---

<sup>\*</sup> Research Engineer, AIAA Member.

<sup>†</sup> Graduate Research Assistant.

<sup>‡</sup> Professor, AIAA Associate Fellow.

## I. Introduction

THE present paper focuses on the role and coupling mechanisms of direct high-frequency actuation on a plane turbulent shear layer. The interaction between the shear layer and actuation is provided through the wall boundary layer just upstream from the separation point, as shown schematically in Figure 1. High-frequency actuation is imposed by a train of counter-rotating vortex pairs that are ejected into the boundary layer. Depending on the injection frequency and their circulation, the initial interaction zone between the high-frequency vortices and the shear layer can be varied. The imposed vorticity can be completely contained within the boundary layer and carried into the shear layer without impacting the free stream, or the vortices can protrude through the boundary layer and interact with the initial shear layer from the free stream. The main objective of the present work is to gain a better understanding of the role of such actuation in the short- and long-range domain of the shear layer. An example of the significant effect of the high frequency actuation on the redistribution of energy within the shear layer is shown in Figure 2. Power spectra of the streamwise velocity fluctuations are plotted at an arbitrary point in the shear layer for the baseline (unforced) and the shear layer forced at frequency nominally an order of magnitude higher than the naturally-evolving frequency of the baseline flow. The spectrum of the unforced layer exhibits a strong peak at the natural frequency  $f_n$ . As the actuation is applied, the corresponding spectrum shows several distinctions. First, it shows the focused peak at the actuation frequency ( $\sim 10f_n$ ), but there is also a broad range of high frequencies having increased energy (marked as zone B). Simultaneously with the increase of energy at the high frequencies, there is a decrease of energy at large scales (marked as A). Such energy deficit seems to suppress formation of the coherent structures at the natural frequency and there is no peak at  $f_n$  in the forced flow. Overall, there is a range of large scales with lowered energy in the forced flow while at the same time a range of small scales enhances its energy, with the crossover frequency  $f_c$ , as denoted on the plot.

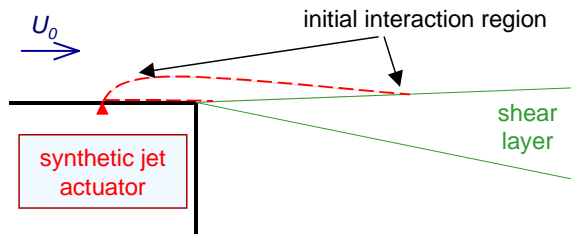


**Figure 1. The single-stream shear layer and vorticity manipulation using direct high-frequency actuation.**

The role of the coherent vortical structures in the evolution of plane shear layers has been traditionally investigated in two-stream flows (dating back to the pioneering works of Brown and Roshko<sup>1</sup> and Winant and Browand<sup>2</sup>) and relatively little work has been devoted to single-stream shear layers. A single stream layer formed by a backward step blower was investigated by Wygnanski and Fiedler<sup>3</sup>. In order to avoid an extensive transition region these authors inserted a trip wire upstream of the shear layer and observed a fundamentally different flow development from previous studies and indicated the significance of initial conditions for flow development (the connection between flow development and the trip wire was confirmed in later experiments). Using the same facility, Champagne, Pao, and Wygnanski<sup>4</sup> altered the initial conditions of the flow producing different results for the growth rate of the shear layer from Wygnanski and Fiedler<sup>3</sup> but replicating the results of other experimenters. Hussain and Zaman<sup>5</sup> also investigated a single stream shear layer in a similar experimental setup to characterize the coherent structures with the addition of an entrainment flow normal to the free stream downstream of the step. Morris and Foss<sup>6</sup> also studied an unforced single stream shear layer in a wind tunnel with a similar entrainment flow apparatus as that of Hussain and Zaman<sup>5</sup> and focused on the initial development of the shear layer conducting experiments where the Reynolds number was an order of magnitude larger than in the present work.

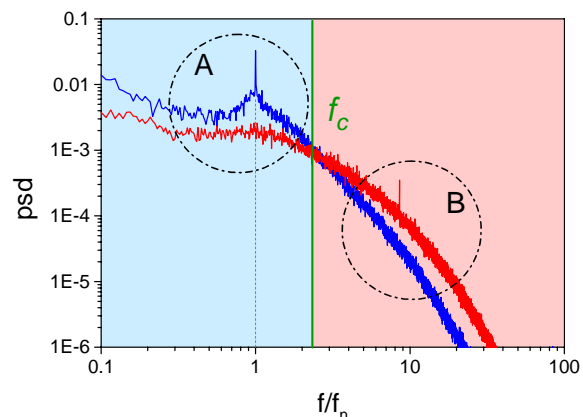


**Figure 2. Power spectra of the streamwise velocity showing the effect of direct high-frequency actuation: unforced (blue) with a spectral peak at the natural frequency  $f_n$ , and forced (red) with a spectral peak at the actuation frequency [ $O(10f_n)$ ]**

The earlier works on the separating single stream shear layer from a backward-facing step have dealt primarily with the issues of separation and reattachment. In a review article of flow separation and reattachment downstream of a backward-facing step Eaton and Johnson<sup>7</sup> also compare the single- and two-stream shear layers and cite several investigations in which the measured growth rate of the two flows are comparable. Their ultimate conclusion is that

in the near field a reattaching (single-stream) shear layer is indeed very similar to a two-stream shear layer in terms of the overall structure and turbulence characteristics. Similar to the trip wire used in Wygnanski and Fiedler<sup>3</sup>, Otugen<sup>8</sup> used passive methods to alter flow development such as changing the geometry (backward-facing step expansion ratio or ratio of step height to test section height) which when increased led to a decrease in reattachment length. Active flow control methods are common; Nagib, Reischel, and Koga<sup>9, 10</sup> used periodic oscillations of a mechanical flap to control reattachment length. In a numerical study, Kaiktsis and Monkewitz<sup>11</sup> employed a combination of suction on the step face and blowing downstream of the step to destabilize the flow. They concluded that their strategy works well for more-easily simulated laminar flows but uncertainty is expressed concerning the application to the more relevant case of turbulent flow over the backward-facing step. Chun and Sung<sup>12</sup> and Chun, Lee, and Sung<sup>13</sup> used an acoustic speaker to actuate the flow and minimize the reattachment length. This work produced increased mixing in the near field and enhanced entrainment by affecting the large structures created by the natural frequency of the layer.

As noted above, the present paper focuses on the role and coupling mechanisms of direct high-frequency actuation on a plane turbulent shear layer where the interaction between the shear layer and synthetic jet actuation is effected through the boundary layer just upstream of separation (Figure 1). Some of the aspects of the interactions between synthetic jets and the free stream were already discussed by Vukasinovic, Lucas, and Glezer<sup>14</sup>, and were also the subject of other investigations.<sup>15, 16, 17</sup> Besides the effect of the pure high-frequency actuation, the effect of concomitant excitation of the low- and high-frequency motions is studied with the emphasis on the indirect formation of large coherent structures that arise in the flow as a consequence of the modulated actuation signal. The experimental setup and procedures are described in Section II. Section III characterizes the baseline (unforced) flow. The effects of high-frequency actuation using a pure single-frequency waveform are described in Section IV, while the effects of the simultaneous excitement of small- and large-scales are presented in Section V. Finally, the transient dynamics of the large-structure formation is further discussed in Section VI.

## II. Experimental Setup and Procedures

The experiments are conducted in a low-speed, closed return wind tunnel that is specifically designed for high-

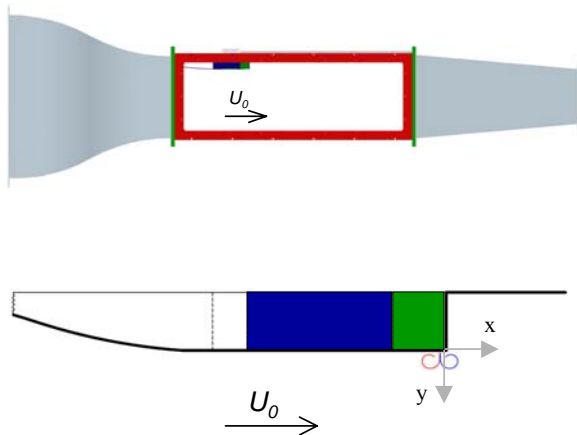


**Figure 3. The wind-tunnel test section and the backward-facing step flow configuration on the upper surface.**

resolution PIV measurements. Figure 3 shows a scaled schematic diagram of the contraction, test section, and diffuser of the wind tunnel. The test section has transparent walls on three sides and measures  $25.4 \times 40.6 \times 132.1$  cm. The tunnel has no screens and is equipped with a minimal number of honeycomb sections to avoid PIV seeding blockage and accumulation. Nonetheless, the measured free stream turbulence intensity is less than 0.5% over the entire range of tunnel speeds. The shear layer is generated by the flow separation off the edge of a backward-facing step, thus representing a canonical single-stream shear flow. The step spans the full width of the test section and its height relative to the wall of the test section is  $H = 50.8$  mm. Although the step is built in the upper wall of the test section (Figure 3), the results are presented in a flipped field of view.

A six-module synthetic jet actuator is integrated into the step surface. The orifice of each individually-controlled module measures  $0.38 \times 18.3$  mm and the spanwise spacing between adjacent orifices is 1.9 mm (the actuators span about 95% of the step). The actuator orifices are 8 mm (21 orifice widths) upstream of the step edge and the jets issue normal to the step surface. Figure 3 also shows the close-up schematics of flow geometry. The operating frequency of the actuators is within the range  $St_H = 2.2 - 8.1$  for the tested free stream flow. Each module is calibrated outside of the test section by measuring cross stream velocity distributions over the exit orifice using hot wire anemometry. A movable miniature pressure probe is used for assessing the module performance *in-situ* between the runs. The input to the actuators is a time-harmonic carrier signal and two operating frequencies are selected such that  $St_H = 3.31$  and  $7.36$  over a range of jet momentum coefficients. The jet momentum coefficient  $C_\mu = \rho U_j^2 b_j / (\rho U_0^2 H)$  is varied between  $4 \cdot 10^{-3}$  and  $69 \cdot 10^{-3}$  (the average jet velocity  $U_j$  is measured 1 mm downstream from the orifice and  $b_j = 0.38$  mm). Amplitude-modulated forcing was accomplished using square wave modulation at a modulation frequency  $f_{AM}$  that is an order

of magnitude lower than the carrier ( $0.18 < St_{AM} < 1.1$ ). The boundary layer over the step surface is tripped well upstream of the edge (using a 1 mm diameter trip wire) and the flow over the actuators is turbulent. In the absence of actuation, the boundary layer thickness at the step edge is 4.7 mm, and the momentum thickness is  $\theta_0 = 0.35$  mm with Reynolds number  $Re_H \approx 43,000$  (based on the step height  $H$  and the free stream velocity  $U_0$ ) and  $Re_{\theta_0} \approx 470$  (based the momentum thickness at the step edge).

The flow field within the domain  $-0.5 < y/H < 0.5$  and  $-0.5 < x/H < 2.5$  (in the vertical,  $x$ - $y$  plane) is measured using high-resolution particle image velocimetry (PIV) having a nominal imaging resolution of  $26.9 \mu\text{m}/\text{pixel}$ . The PIV measurements are taken over eleven partially overlapping windows and the CCD camera and part of the laser-sheet optics are mounted on computer-controlled traverse mechanisms. Measurements of the interaction between the high-frequency vortex pairs and the cross flow were taken at finer resolution ( $6.5 \mu\text{m}/\text{pixel}$ ). Spectral analysis of the flow was obtained from single-sensor hot-wire anemometry.

### III. The Baseline Flow

Cross-stream distributions of the ensemble-averaged, streamwise velocity component  $\bar{U}$  at eight downstream locations  $x/H = 0.1, 0.2, 0.25, 0.5, 0.75, 1, 1.5,$  and  $2$  are plotted in Figure 4a. The mean flow evolves slowly in the downstream direction, and the finite step height and a presence of the wall affect the velocity profiles as weak, recirculating flow is formed below the low stream edge of the shear layer. As the boundary layer evolves into the single-stream shear layer, there is an asymmetry in its cross stream spreading owing to the entrainment on the low-speed (wall) side, and as a result, the shear layer spreads more on this side. Two global parameters that characterize the spreading of the shear layer are shown in Figure 4b, namely the streamwise variation of the cross stream width  $b$  and momentum thickness  $\theta$ . The shear layer width is defined as the difference between cross-stream elevations where the local mean velocity is 95% and 5% of  $U_0$ . These data show that the streamwise growth rate of the layer is measured by  $db/dx \sim 0.179$  and  $d\theta/dx \sim 0.032$ , which are comparable to similar measurements in two-stream shear layers<sup>18, 19</sup> and the single-stream shear layer<sup>5, 6</sup>.

Next, the receptivity to and amplification of “natural” disturbances are considered. For that purpose, power spectra of the velocity fluctuations are measured across the shear layer at eight streamwise locations through  $x/H = 1.4$ . Figure 5 shows contour plots of the spectral power at the frequencies  $f = 50, 100, 200,$  and  $300$  Hz. As expected, the domains of maximum amplification move downstream with the decrease in frequency. For instance, motions at 300 and 200 Hz are the most amplified around  $x/H = 0.4$  and  $0.6$ , respectively while the maximum amplification of motions at lower frequencies appear to peak outside of the measurement domain.

### IV. Direct High-Frequency Actuation

The effect of high-frequency actuation on the evolution of the shear layer is demonstrated in Figure 6 for forcing at  $St_H = 7.36$  and  $C_\mu = 2.6 \times 10^{-2}$ . The full-field plot shows the mean vorticity contour with equidistant mean velocity profiles. The mean flow does not exhibit a significant departure from the baseline flow with slowly evolving velocity profiles in the downstream direction. The only notable difference in the mean flow is a slight increase in vorticity immediately downstream from the jet orifice. In order to isolate the high-frequency structures that are imposed in the flow through the boundary layer, phase-locked velocity measurements are taken within the

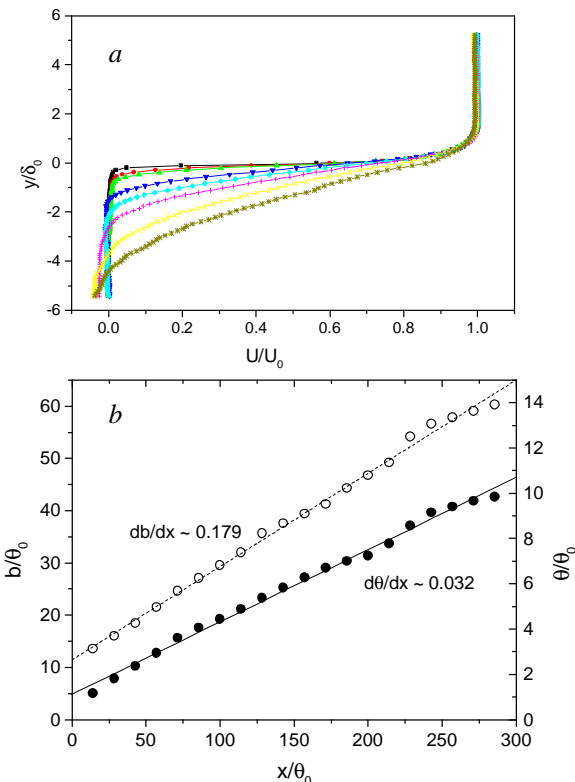


**Figure 4. a) Cross stream distributions of the streamwise velocity at  $x/H = 0.1$  ( $\blacksquare$ ),  $0.2$  ( $\bullet$ ),  $0.25$  ( $\blacktriangle$ ),  $0.5$  ( $\blacktriangledown$ ),  $0.75$  ( $\blacklozenge$ ),  $1$  ( $+$ ),  $1.5$  ( $\times$ ), and  $2$  ( $*$ ). b) The corresponding streamwise variation of the shear layer width  $b$  and momentum thickness  $\theta$ .**

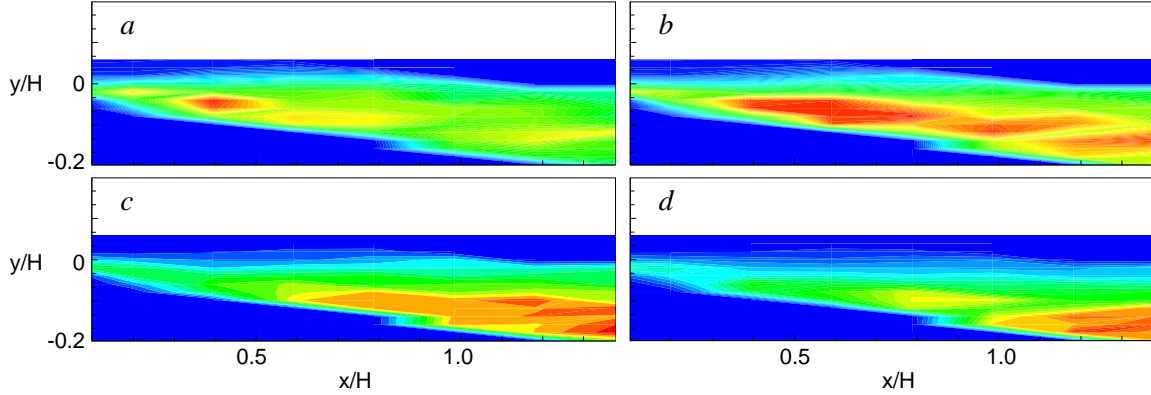


**Figure 5. Amplification of spectral components of the streamwise velocity fluctuations in the baseline (unforced) shear layer:  $f = 300$  Hz (a), 200 Hz (b), 100 Hz (c), and 50 Hz (d). Contour levels:  $1E-3$  to  $2E-2$ .**

framed region for the same flow conditions. The measurements are phase-locked to the high-frequency actuation signal at (arbitrary) phase  $\phi = 140^\circ$ . The vorticity concentrations are shown in the top plot of Figure 6. These measurements clearly show a vortex train along the upper boundary of the shear layer which retains its phase coherence up to approximately  $x/H = 0.5$  and therefore a significant coupling between these vortices and the shear layer is expected farther downstream. As mentioned earlier in connection with Figure 1, the circulation of these vortices can be manipulated and the initial interaction zone between the jets and the shear layer altered. Furthermore, since the vortex train is formed entirely out of clockwise vortices, it is instructive to assess the dynamics of the vortex pair from the point of its injection into the flow. For that purpose, maximum flow field resolution is used to yield a field of view that spans approximately sixteen orifice widths with vector field resolution of  $b_j/4$ . These PIV measurements are taken phase-locked with the actuation signal in phase increments of  $\Delta\phi = 20^\circ$  under the same flow conditions as in Figure 6. Vorticity concentrations at every second phase are shown in Figure 7. The initial formation of the vortex pair is shown in figure 7a ( $\phi = 100^\circ$ ). The vortices are not visible at the beginning of the cycle due to the inherent delay between input signal and the motion of the piezoelectric disks. It is apparent in this early stage of the synthetic jet cycle that the structure with clockwise (CW) vorticity is dominant due to the presence of a cross flow [note the significant spreading of CW vorticity while the counterclockwise (CCW) remains concentrated in a small region at the orifice]. As the jet cycle continues (Figure 7b,  $\phi = 140^\circ$ ) the CCW structure which is also weakened by the CW vorticity in the boundary layer is moved over and is wrapped around the CW structure. The jet cycle proceeds through the next two phases,  $\phi = 180^\circ$  and  $220^\circ$  (Figures 7c and 7d, respectively) where the CW structure becomes larger and more concentrated and the CCW structure continues to wrap around the CW structure nearly surrounding it (except near the wall) by  $\phi = 220^\circ$ . The expulsion cycle concludes after half of the entire cycle (between  $\phi = 260^\circ$  and  $300^\circ$ , Figures 7e and 7f, respectively). At this point, the CCW vortex begins to form a more coherent structure that is significantly less concentrated than the corresponding CW structure and the two structures move downstream (the CW vortex is advected slower in the wall region). During the remaining part of the cycle, the CCW structure dissipates much faster than the CW vortex and exits the measurement domain after approximately one full cycle ( $\Delta\phi = 360^\circ$ , Figure 7a).

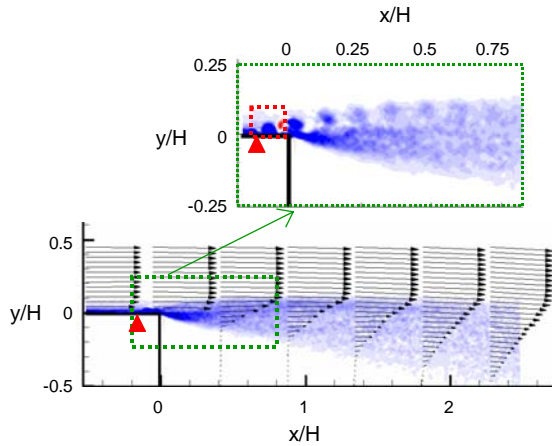


**Figure 6. The mean vorticity field with cross stream velocity distributions the forced shear layer ( $St_H = 7.36$ ,  $C_\mu = 2.6 \times 10^{-2}$ ) and a zoomed-in phase-locked image of the vorticity near the step edge. Vorticity  $\zeta_z$  ( $s^{-1}$ ) contour levels: -2500 to 2500.**

At the same time, the CW structure is advected down to  $x = 8b_j$  and begins to lose coherence when the next vortex pair is distinctly visible at the origin. Therefore, it is expected that the CW vortex has a dominant impact on the separating flow off the step just downstream from the measured domain (at  $x \approx 21b_j$ ).

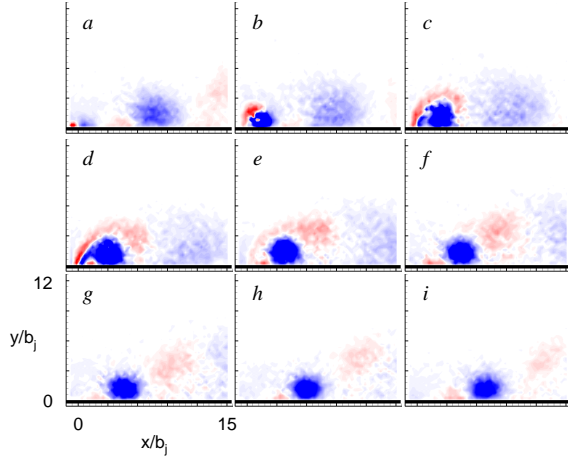


**Figure 7. Phase-locked vorticity concentrations showing the interaction of the jet vortex pair with the cross flow. The actuation frequency is  $f = 2000$  Hz and the jet orifice ( $b_j = 381 \mu\text{m}$ ) is located at  $x = y = 0$ . The phase angles relative to the driving frequency are  $\phi = 100^\circ$  (a),  $140^\circ$  (b),  $180^\circ$  (c),  $220^\circ$  (d),  $260^\circ$  (e),  $300^\circ$  (f),  $340^\circ$  (g),  $20^\circ$  (h), and  $60^\circ$  (i). Vorticity contour levels are the same as in Fig.6.**

scales with increased energy. The center of the range, namely the crossover frequency at 5 kHz ( $St = 18.4$ ) is shown in white. The results of Vukasinovic et al.<sup>14</sup> indicated that the region of high  $k$  induced by the advected vortical train terminates downstream of  $x/H = 0.1$  for  $C_\mu = 4 \cdot 10^{-3}$  due to the direct interaction between the high-frequency vortices and shear layer through the oncoming boundary layer. The vortices do not protrude through the boundary layer, are carried directly into the separation region, and as a consequence, the average measure of  $k$  becomes lower than in the unforced flow immediately after this short interaction region.

The work of Vukasinovic, Lucas, and Glezer<sup>14</sup> showed that the average turbulent kinetic energy  $k$  becomes lower in the high-frequency forced than in the baseline shear layer in spite of significant local increase immediately downstream from the jet injection. To further investigate the transfer of energy in the forced flow, spectral analysis is conducted based on the hot wire measurements of the streamwise velocity fluctuations. The measurements are taken at eight cross sections of the shear layer between  $x/H = 0.1$  and 1.38. Four different forcing conditions are analyzed at  $C_\mu \cdot 10^{-3} = 4, 26, 51,$  and  $69$  for  $St_H = 7.36$ . As discussed in connection with Figure 2, the crossover frequency  $f_c$  is defined as the frequency up to which the energy content of the large scales is lowered as a consequence of the high-frequency forcing and above which the energy of the small scales is enhanced in the forced flow (relative to the unforced flow). For this reason the spectral results in Figure 8 are shown as contour plots of the crossover frequency  $f_c$ . An increase in the magnitude of  $f_c$  [up to 10 kHz ( $St = 37$ ), represented by increasingly intense blue] implies an increase of a range of scales with decreased energy in the forced flow. Similarly, decreasing  $f_c$  [down to 1 Hz ( $St = 0.0037$ ), represented by increasingly intense red] indicates increasing range of

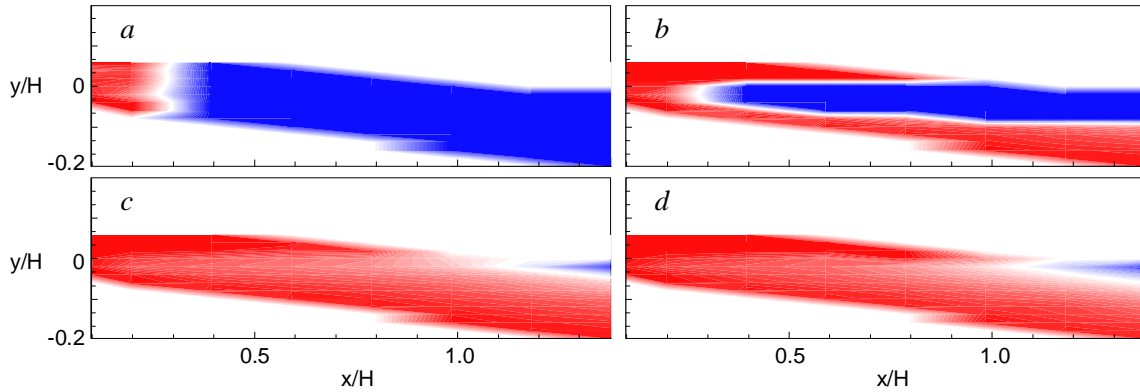


**Figure 8. Contour of the crossover frequency  $f_c$  for the forced shear layer ( $St_H = 7.36$ ):  $C_\mu \times 10^3 = 4$  (a), 26 (b), 51 (c), and 69 (d). Contour levels: 1E0  1E4.**

The present spectral results are shown in Figure 8a. It is seen that initial suppression of energy across the large scales spreads almost uniformly across the shear layer and that a range of affected scales rapidly increases toward the small scales. In other words, an initial narrow-band increase in energy of the small scales is rapidly dissipated with downstream distance and the energy over all scales is already suppressed downstream of  $x/H = 0.2 - 0.3$ . Therefore, the overall effect of the high-frequency forcing can be described as having a stabilizing impact in terms of the overall suppression of the fluctuations. The earlier work of Vukasinovic et al.<sup>14</sup> showed that even as  $C_\mu$  increases, there is a streamwise location at which an average measure of the turbulent kinetic energy  $k$  in the forced flow is ultimately lower than in the unforced flow and that this location moves downstream with  $C_\mu$ . The contour plots of  $f_c$  in Figure 8 suggest that the transfer of energy among the scales is significantly altered with the increase in  $C_\mu$ . Already at  $C_\mu = 2.6 \cdot 10^{-2}$  (Figure 8b), an initial sharp increase of the range of scales with lower energy is visible

in the center of the shear layer but both the high- and low-speed edges show overall increase in  $k$ . The high-speed edge of high  $k$  is induced by the advection of the actuator jet vortices, while the low speed edge is induced by the increased spreading of the shear layer. As the forcing vortices dissipate downstream,  $k$  in the upper branch becomes lower across all scales. In the lower branch, the dissipation of energy in the smaller scales occurs farther downstream and full reduction over all scales is not detected in the measurement domain. Figures 8c and d show no substantial broadening of the low-energy spectral bands within the shear layer. The strongest decrease in energy occurs within the center of the shear layer and spreads slowly towards its edges. The increased energy due to the extended interaction region feeds the energy of the small scales, while increased spreading towards the low speed side increases the energy content across all scales. It appears that the most significant reduction of turbulent kinetic energy occurs if the high-frequency control is contained within the wall boundary layer. Otherwise, there is a redistribution of energy across the scales, which tends to decrease the energy over a broad band of scales within the core of the shear layer, but increase the energy at the small scales near its edges. Therefore, it can be argued that the energy that is fed into the shear layer at small scales through the interaction region enhances spatial transfer of energy from large scales in the bulk of the shear layer to the engulfed fluid at the low-speed side.

Finally, the impact of lower forcing frequency on energy redistribution within the shear layer is investigated. For that purpose, the flow is forced at  $St_H = 3.31$  while  $C_\mu = 2.23 \cdot 10^{-2}$ . The corresponding contour plot of  $f_c$  is shown in Figure 9. As expected, the energy that is fed into the shear layer at larger scales dissipates over longer downstream distance and as a consequence, the transition to the domain where the energy is diminished over all scales is pushed farther downstream. Otherwise, the energy balance across the shear layer is similar to that at higher  $St_H$ . Four profiles of the crossover frequency  $f_c$  for the two Strouhal numbers are also plotted in Figure 9 for  $x/H = 0.2, 0.6, 1,$  and  $1.38$ . The streamwise increase in the magnitude of the crossover frequency is seen in both cases and it is interesting that the profiles on near the low-speed edge are very similar indicating similar energy transfer to the entrained fluid.

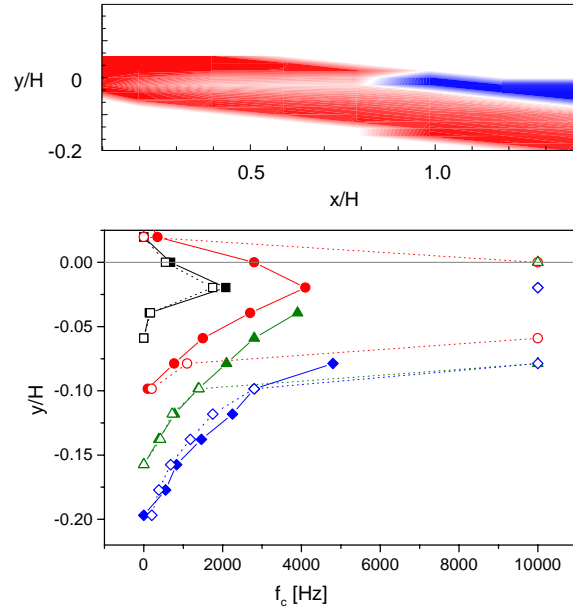


**Figure 9. Contours of the crossover frequency  $f_c$  for the forced shear layer ( $St_H = 3.31$ ,  $C_\mu = 2.23 \times 10^{-2}$ ) and cross stream distributions of  $f_c$  (---) at  $x/H = 0.2$  ( $\square$ ),  $0.6$  ( $\circ$ ),  $1$  ( $\Delta$ ), and  $1.38$  ( $\diamond$ ) along with the corresponding distributions for  $St_H = 7.36$  and  $C_\mu = 2.46 \times 10^{-2}$  (—, solid symbols). Contour levels are the same as in Fig.8.**

## V. Concomitant High- and Low-Frequency Actuation

Although the high-frequency actuators operate at the frequencies that are an order of magnitude higher than the naturally-evolving frequencies in the flow, they can be also used to manipulate frequencies that are comparable to

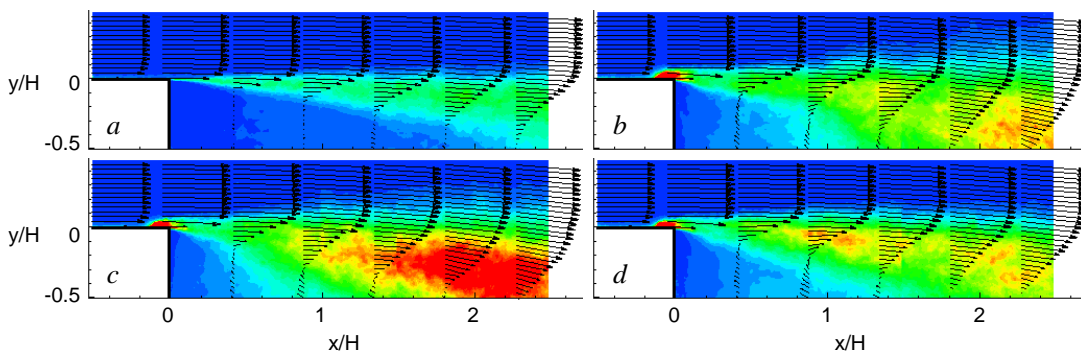


**Figure 10. Contours of the turbulent kinetic energy  $k$  with cross stream distributions of the mean velocity for the baseline flow (a) and the forced flow  $St_{AM} = 0.184$  (b),  $0.364$  (c), and  $0.736$  (d). TKE  $k$  ( $m^2/s^2$ ) contour levels: 0 20.**

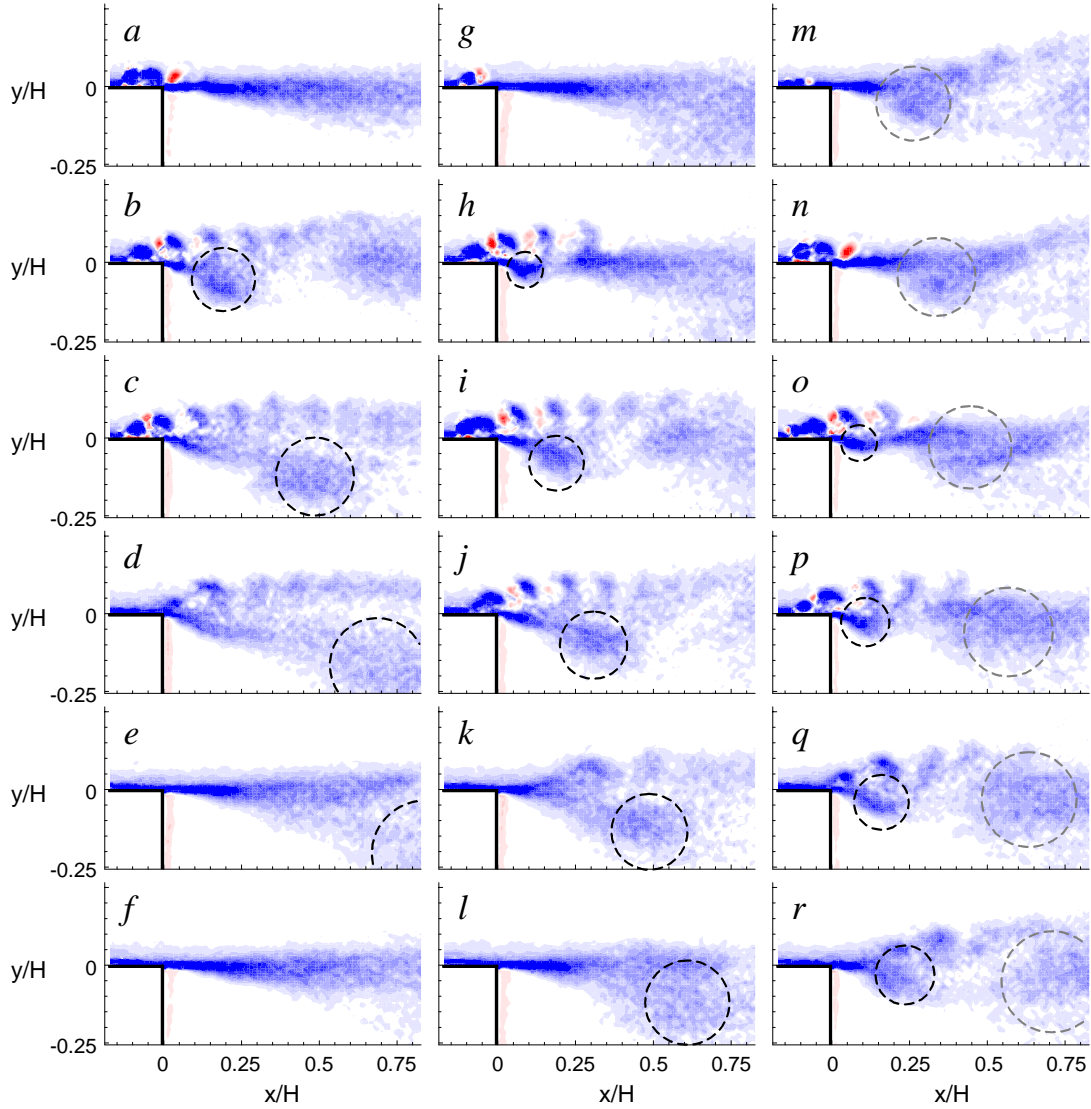


**Figure 11. Phase-locked vorticity concentrations for  $St_{AM} = 0.184$  (a-f),  $0.364$  (g-l), and  $0.736$  (m-r) for modulation phase angle  $\phi = 20^\circ$  (a, g, m),  $80^\circ$  (b, h, n),  $140^\circ$  (c, i, o),  $200^\circ$  (d, j, p),  $260^\circ$  (e, k, q), and  $320^\circ$  (f, l, r). Vorticity contour levels are the same as in Fig.6.**

the “natural” frequencies. Large-scale motions are introduced by low-frequency amplitude-modulation of the high-frequency signal. Wiltse and Glezer<sup>20</sup> first demonstrated experimentally that the spectral sidebands of the time harmonic, high-frequency actuation waveform that are introduced through amplitude modulation induce coherent motions at the modulation frequency. This approach adds large-scale motions to the directly induced small-scale motions in the flow and has been used in other flow control applications to the shear flows<sup>21,22</sup>.

In the present experiments this approach is applied to actuation at  $St_H = 7.36$  and  $C_\mu = 26 \times 10^{-3}$  using 50% duty cycle square-wave amplitude modulation at modulation frequencies:  $St_{AM} = 0.184$ ,  $0.364$ , and  $0.736$ . As a result, the nominal high-frequency actuation is active only during the first half of the modulation period. In the presence of modulation, the jet velocity is adjusted so that it is unchanged. Spatial distributions of turbulent kinetic energy  $k$  measured within the full-field PIV domain ( $-0.5 < x/H < 2.5$ ) are shown in Figures 10b-d (the baseline flow is shown for reference in Figure 10a). These concentrations indicate significant enhancement in the cross stream spreading of the forced shear layer that is accompanied by a substantial increase in  $k$ . However, the zones of maximum enhancement of  $k$  are directly related to the time scale of  $St_{AM}$ . Since the characteristic formation time of the large structure at the modulation frequency increases with the decrease in  $St_{AM}$ , the peak  $k$  moves downstream and is

centered about  $x/H = 2$  for  $St_{AM} = 0.364$  (Figure 10c), about  $x/H = 1$  for  $St_{AM} = 0.736$  (Figure 10d), and it is outside the measurement domain for the lowest  $St_{AM}$  (Figure 10b).

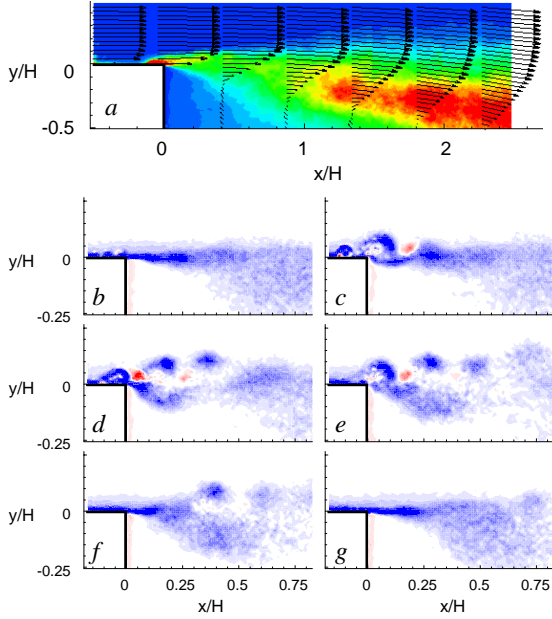


**Figure 12.** Contours of the turbulent kinetic energy  $k$  for at  $St = 3.31$  and  $St_{AM} = 0.364$  (a), and corresponding phase-locked vorticity concentrations for modulation phase angles  $\phi = 20^\circ$  (b),  $80^\circ$  (c),  $140^\circ$  (d),  $200^\circ$  (e),  $260^\circ$  (f), and  $320^\circ$  (g). Vorticity contour levels are the same as in Fig.6 and TKE-levels are same as in Fig. 10.

high-frequency vortex pairs are injected into the free stream, while the large structure grows along the lower bound of the shear layer (marked by the dashed circle). By the end of the half of the modulation cycle ( $\phi = 180^\circ$ ) the large vortex still grows and starts to move out of the field of view. Following the end of the actuation (Figure 11d), the upstream boundary layer recovers and the onset of shear layer temporarily returns to the unforced state (Figures 11e and 11f). The full interaction between the small-scale vortices that are formed by the actuation and the large vortical structure is more pronounced at  $St_{AM} = 0.364$  (Figures 11g-l). Following the termination of the actuation (Figure 11j), the high frequency vortex train partially coalesces with the large vortex while the remaining high-frequency vortices are advected downstream and may form the braid region between two consecutive large structures. The growth of the large vortex depends on the modulation period and for  $St_{AM} = 0.736$  (Figures 11m-r) it is considerably

Although there is abundant experimental evidence of indirect excitation of the large-scale structures via amplitude modulation of the high-frequency actuation waveform, the physical mechanisms of their formation has not been investigated in detail. The earlier work of Vukasinovic, Lucas, and Glezer<sup>14</sup> showed that the large coherent structures are formed by the transient motions near the flow separation and that they are associated with the onset and termination of the modulation duty cycle. The dynamics of the large coherent structure formation is further investigated here for the three modulation cases of Figure 10 ( $St_{AM} = 0.184, 0.364,$  and  $0.736$ ). The PIV measurements are taken phase-locked to the modulation period with phase increment  $\Delta\phi = 20^\circ$  and the field of view is comprised of two partially overlapping windows that are centered about the step edge. Figure 11 shows six phase-averaged vorticity maps at phase increments of  $60^\circ$  relative to the modulation waveform for the three modulation frequencies (the 50% duty cycle square-wave modulation begins at  $\phi = 0^\circ$ ). These images show the formation of a large CW vortical structure downstream of the step. Although the initial rollup of this vortex appears to be independent of  $St_{AM}$ , there is a clear difference in its dynamics afterwards. The lowest  $St_{AM}$  allows for the longest formation time of the large structure and simultaneously with its formation, a train of high-frequency CW vortices is advected along the high-speed edge of the shear layer. At  $\phi = 80^\circ$  (Figure 11b) eight

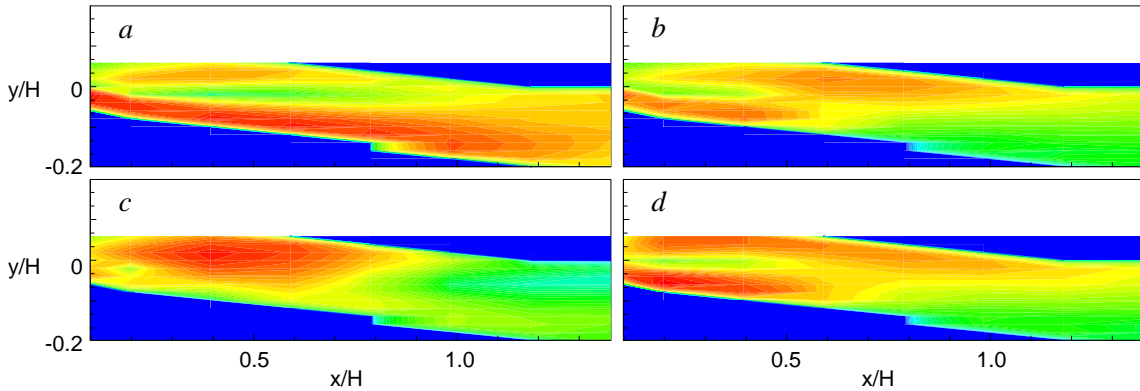


**Figure 13.** Contours of the spectral component at the modulation frequency  $f_{AM}$ .  $St = 7.36$  and  $St_{AM} = 0.184$  (a),  $0.364$  (b), and  $0.736$  (c), and  $St = 3.31$  and  $St_{AM} = 0.364$  (d). Contour levels:  $1E-3$  to  $1E0$ .

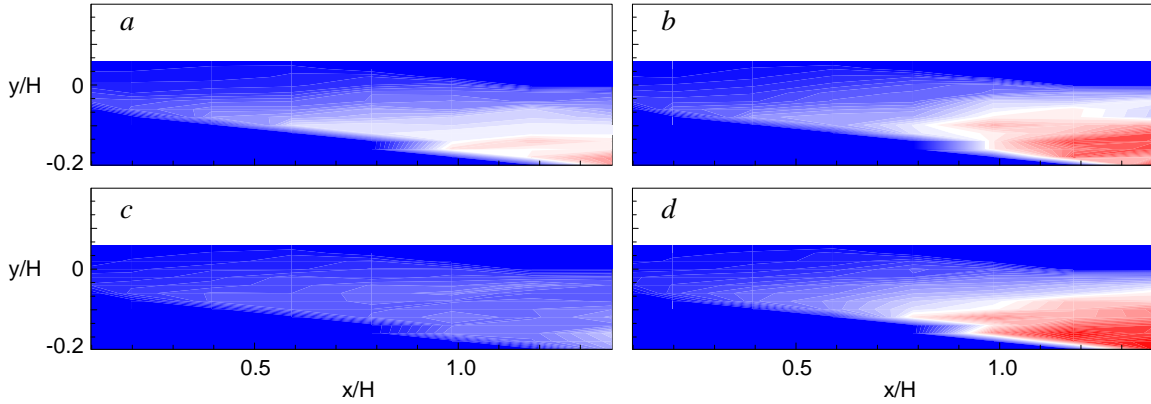


**Figure 14.** Contours of the spectral component  $f_{AM}/2$  for  $St = 7.36$  and  $St_{AM} = 0.184$  (a),  $0.364$  (b), and  $0.736$  (c), and  $St = 3.31$  and  $St_{AM} = 0.364$  (d). Contour levels:  $1E-3$  to  $4E-2$ .

smaller and its interaction with the high-frequency vortex train starts already at  $x/H = 0.2$  (Figures 11q and 11r). By the time that next modulation period starts, large structure from the previous period still interacts with the vortex train within the field of view (marked with full circle). These data show that the transients associated with the onset and termination of the modulation cycles are the primary trigger for the formation of the large vortical structures at the modulation frequency and indicate that the large vortex formation is primarily affected by the modulation cycle and is almost independent of changes in the exact carrier (high) frequency. To check this, the carrier frequency was changed to  $St_H = 3.31$  while the modulation frequency is kept at  $St_{AM} = 0.364$  (similar to  $St_H = 7.36$ , Figures 11g-l). Figure 12 includes contours of  $k$  (Figure 12a, cf. Figure 10c) and phase-locked vorticity concentrations that correspond to the phases of Figures 11g-l (Figure 12b-g). Both the time- and phase-averaged fields are strikingly similar. For example, both fields exhibit maximum  $k$  about  $x/H = 2$ . Although there are some difference in the details of the flow field (e.g., at the lower  $St_H$ , the high-frequency vortices are somewhat larger in size and only four high-frequency actuation cycles are completed during the active half of the modulation period, Figure 12e), the dynamics of the large vortex is unchanged. As the first CW vortex disrupts the boundary layer, the large vortex begins to form off the step edge (Figure 12c) and its subsequent growth is similar to  $St_H = 7.36$  (note the similarity between Figures 11k and 12f and Figures 11l and 12g).

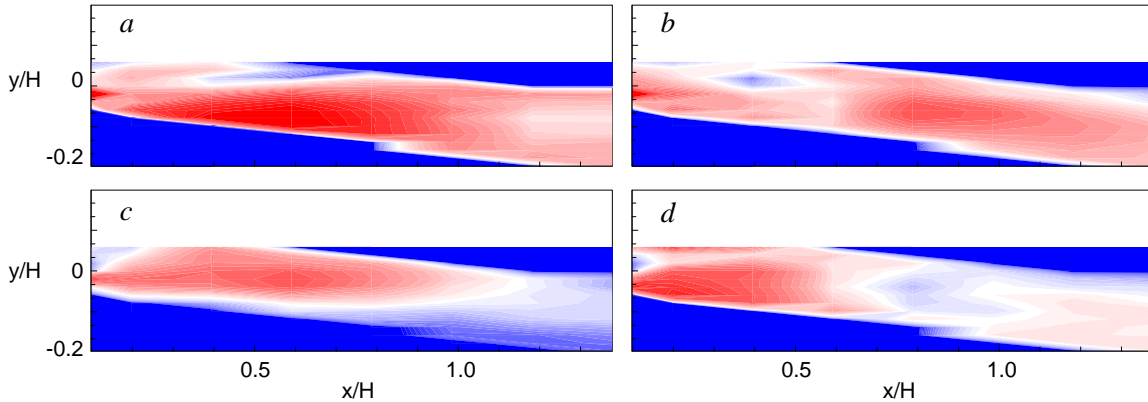


**Figure 15.** Contours of the spectral component  $2f_{AM}$  for  $St = 7.36$  and  $St_{AM} = 0.184$  (a),  $0.364$  (b), and  $0.736$  (c), and  $St = 3.31$  and  $St_{AM} = 0.364$  (d). Contour levels:  $1E-3$  to  $1E-1$ .

Further insight into the dynamics of interaction between the high-frequency vortices and the single large vortex is gained from spectral analysis of time-trace of the streamwise velocity. The measurements are taken for  $St_H = 7.36$  with  $St_{AM} = 0.184, 0.364,$  and  $0.736$ , and  $St_H = 3.31$  with  $St_{AM} = 0.36$ . The spatial amplification of the velocity fluctuation at the modulation frequency is considered as the large vortex is formed at  $f_{AM}$ . Figure 13 shows spatial distributions of the magnitude of the spectral components at  $f_{AM}$  for the four cases. Each plot shows two branches of amplified  $f_{AM}$ . The lower, more dominant branch corresponds to the trajectory of the large vortex while the upper branch corresponds to the high-frequency vortex train. As implied from the phase-locked measurements, these two regions begin to merge after the completion of the active half of the modulation cycle. Following the merging, the motions associated with  $f_{AM}$  are attenuated as manifested by the decay of the magnitude of spectral energy. Figure

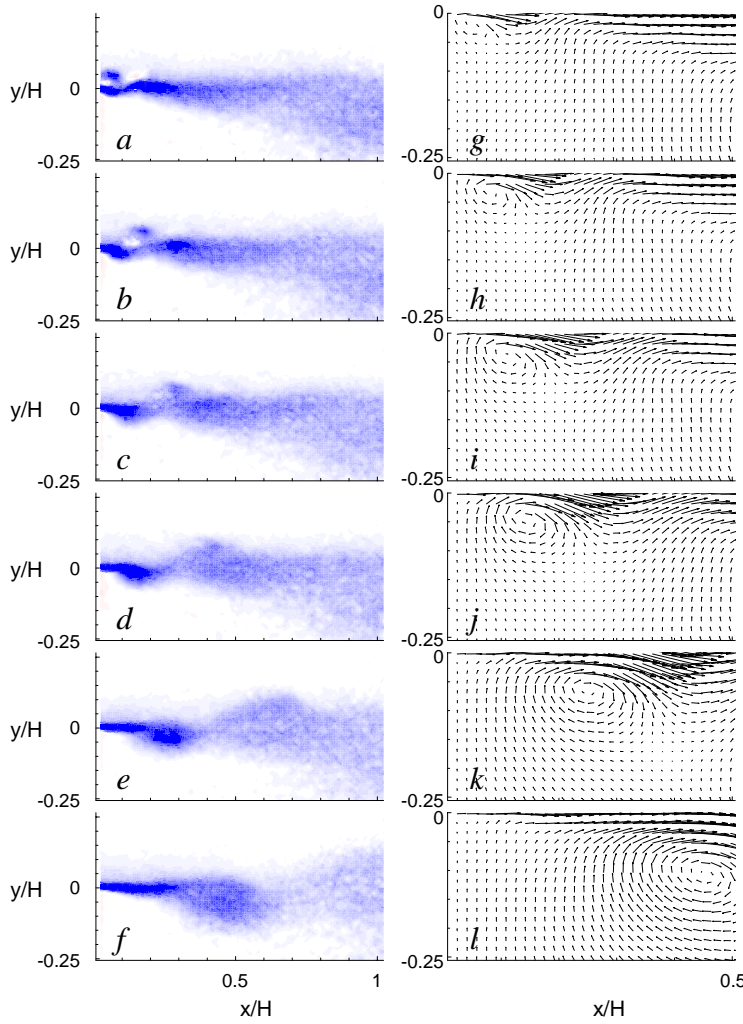


**Figure 16. Phase-locked vorticity concentrations (a-f) and the corresponding magnified velocity field (g-l) for the flow forced at  $St_{AM} = 0.364$  and 5% duty cycle at modulation phase angles  $\phi = 60^\circ$  (a, g),  $80^\circ$  (b, h),  $100^\circ$  (c, i),  $120^\circ$  (d, j),  $160^\circ$  (e, k), and  $240^\circ$  (f, l). Vorticity contour levels are the same as in Fig.6.**

the modulation frequency. Each of the plots exhibits a strong initial peak at  $2f_{AM}$  immediately downstream of the step as the harmonic of the  $f_{AM}$  is inherently induced by the actuation (along with other higher harmonics). Downstream of this domain, the energy at the harmonic decreases but increases again further downstream within the merging domains. Thus, the second peak at  $2f_{AM}$  is seen around  $x/H = 0.7$  for  $St_{AM} = 0.364$  (both  $St_H$ , Figures 15b and 15d), while it is around  $x/H = 0.5$  for  $St_{AM} = 0.736$  (Figure 15c). As expected, the second peak at  $2f_{AM}$  is not present in the field of view for  $St_{AM} = 0.184$  (Figure 15a) since the merging occurs outside of the field of view (Figure 13a).

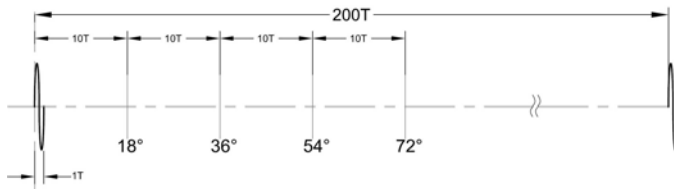
## VI. Transient Dynamics

The formation dynamics of the large vortices is further clarified by minimizing their interactions with the small-scale vortices. This is accomplished by a single-cycle modulation of the high-frequency waveform. For the case of  $St_H = 7.36$  and  $St_{AM} = 0.364$  the modulation duty cycle is taken to be 5%. Under this forcing condition, only a single pair of counter-rotating vortices is formed by the actuator during each modulation cycle. The dynamics of the large vortex is assessed using phase-locked PIV measurements (as described in Figure 11). The measured vorticity field is shown in Figure 16a-f with the emphasis on early stage of formation. Zoomed-in views of the corresponding velocity fields are shown in Figures 16g-l. At  $\phi = 60^\circ$  (Figures 16a and 16g), the small-scale CW vortex has just

13a shows that the merging of the large vortex and the vortex train begins at approximately  $x/H = 1.3$ . In the case of  $St_{AM} = 0.364$  (Figure 13b), the merging occurs around  $x/H = 0.6$ , which corresponds to the dynamics in Figure 11g-l. The existence of two branches is barely visible in Figure 13c because the interaction starts already at  $x/H = 0.25$ , as is evident from Figure 11m-r. Finally, the similarity of Figures 13b and 13d (same  $St_{AM}$  but different  $St_H$ ) demonstrates again the dominant role of the modulation frequency in the evolution of the single vortex. As the energy at the modulation frequency decreases following the merging, it is expected that energy at the subharmonic of the modulation frequency would begin to increase due to the pairing of the large vortices. Contours of the spectral energy at  $f_{AM}/2$  are shown in Figures 14 a-d, corresponding to Figures 13a-d. The gradual streamwise increase in the energy of the subharmonic motions is clearly visible in all plots except  $St_{AM} = 0.736$  where the subharmonic is not distinct. Note that for  $St_{AM} = 0.364$ , the subharmonic motions become significant for  $x/H > 1$  regardless of  $St_H$ .

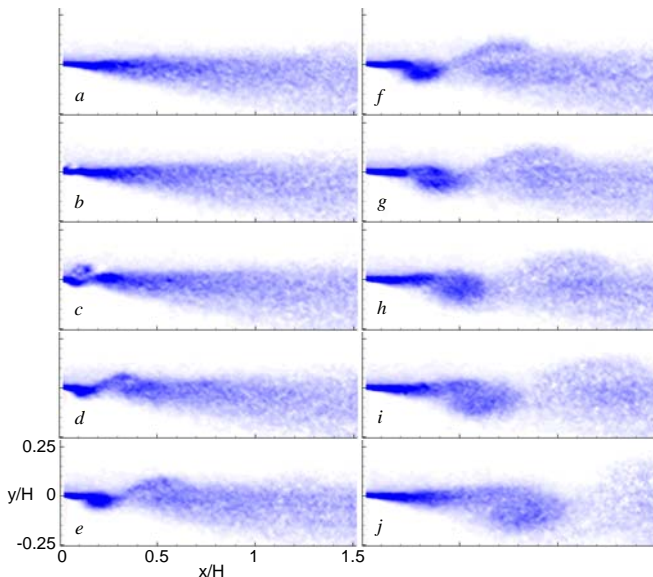
Since the high-frequency vortices coalesce and merge with the large vortices, it is expected that the energy at integer multiples of the carrier frequency would peak in the merging domain. Regardless of the actual  $f_{AM}$ , the merging of the vortices should be marked by the increase in the energy component at  $2f_{AM}$ .

Figure 15 shows spatial distribution of the energy at the first harmonic of the modulation frequency. Each of the plots exhibits a strong initial peak at  $2f_{AM}$  immediately downstream of the step as the harmonic of the  $f_{AM}$  is inherently induced by the actuation (along with other higher harmonics). Downstream of this domain, the energy at the harmonic decreases but increases again further downstream within the merging domains. Thus, the second peak at  $2f_{AM}$  is seen around  $x/H = 0.7$  for  $St_{AM} = 0.364$  (both  $St_H$ , Figures 15b and 15d), while it is around  $x/H = 0.5$  for  $St_{AM} = 0.736$  (Figure 15c). As expected, the second peak at  $2f_{AM}$  is not present in the field of view for  $St_{AM} = 0.184$  (Figure 15a) since the merging occurs outside of the field of view (Figure 13a).



**Figure 17.** Data acquisition timing for  $f_{AM} = 10 \text{ Hz}$  (0.5 % duty cycle), phase locked with the modulation input at  $\phi = 18^\circ, 36^\circ, 54^\circ, 72^\circ$ .

modulation period (Figures 16f and 16l), the large vortex grows substantially with its center advected to  $x/H = 0.5$ . The previous example shows that a *single* small-scale vortex pair is sufficient for excitation of a *single* large coherent structure. When such actuation is applied at the low-frequency periodic rate, it effectively renders the control of shear layer to a sequence of quasi-transient events rather than continuous forcing at low frequencies.



**Figure 18.** Phase-locked vorticity concentrations ( $0 < x/H < 1.5$ ) for  $St_H = 7.36, f_{AM} = 10 \text{ Hz}$  (0.5% duty cycle), at phases  $\phi = 1.8^\circ$  (a),  $3.6^\circ$  (b),  $7.2^\circ$  (c),  $10.8^\circ$  (d),  $14.4^\circ$  (e),  $18^\circ$  (f),  $21.6^\circ$  (g),  $25.2^\circ$  (h),  $28.8^\circ$  (i), and  $36^\circ$  (j). Vorticity contour levels are the same as in Fig.6.

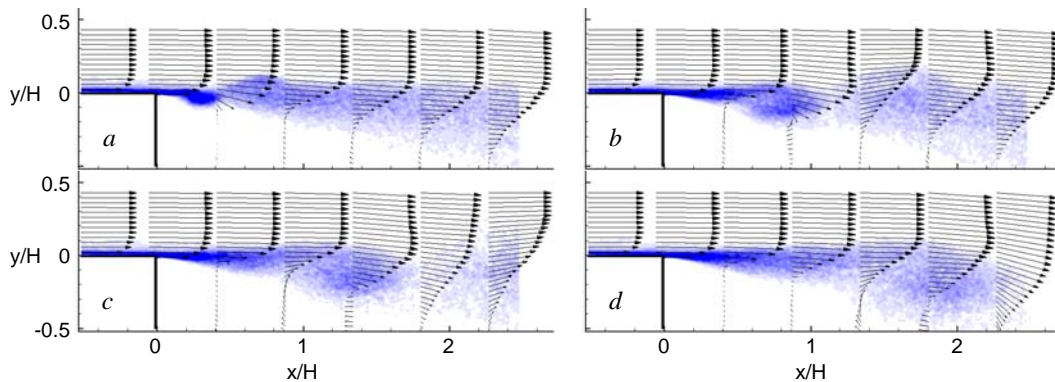


**Figure 19.** Phase-locked vorticity concentrations ( $-0.5 < x/H < 2.5$ ) at  $St_H = 7.36$  with  $f_{AM} = 10 \text{ Hz}$  (0.5% duty cycle), at the phases  $\phi = 18^\circ$  (a),  $36^\circ$  (b),  $54^\circ$  (c), and  $72^\circ$  (d). Vorticity contour levels are the same as in Fig.6.

passed the step edge and this transient passage of the CW vortex disrupts the boundary layer vorticity and results in a large-scale rollup. The rollup of the new vortex entrains nearly stagnant fluid from the region underneath the step as it grows (Figures 16b and 16h). By  $\phi = 120^\circ$  (Figures 16d and 16j), the small CW vortex begins to merge with the large vortex that was created by the transient of the previous modulation cycle. At about 2/3 of the

A schematic for the timing of the data acquisition for the 10 Hz transient case is shown in Figure 17. The duty cycle is decreased such that a single high frequency cycle is produced at the beginning of the modulation cycle or 0.5% for  $f_{AM} = 10 \text{ Hz}$  ( $St_{AM} = 0.0364$ , Figures 18 and 19). Figure 18 shows partial field data ( $0 < x/H < 1.5, -0.25 < y/H < 0.25$ ) of ten phase-averaged images over the initial progression of the large structure created by the single vortex pair in the shear layer. The effect of the actuation is first detected in Figure 18b and is evident by the next phase  $\phi = 7.2^\circ$  (Figure 18c) which occurs after four periods of the high frequency actuation. The break in the layer which forms in front of the vortical structure and precedes it in the downstream flow is first visible at  $\phi = 14.4^\circ$ , Figure 18e (at eight periods) around  $x/H = 0.35$  and is more distinguishable at the rest of the phases in Figure 18. The final view in figure 18 shows the progression of the structure at  $\phi = 36^\circ$  (figure 18j) which occurs after ten periods of the 2000 Hz actuation. Figure 19 shows a full field view of the same forcing scheme as (Figure 18) with phases in increments of ten periods so that

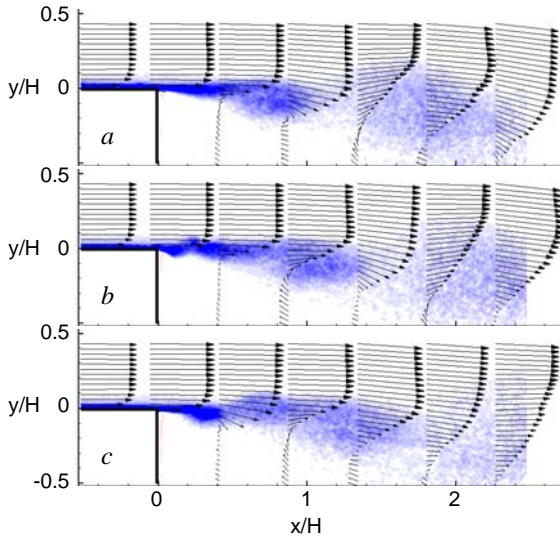


**Figure 20. Phase-locked vorticity concentrations at  $St_H = 7.36 f_{AM} = 100 \text{ Hz}$  (5% duty cycle), at the phases  $\phi = 0^\circ$  (a),  $90^\circ$  (b), and  $180^\circ$  (c). Vorticity contour levels are the same as in Fig.6.**

At  $\phi = 90^\circ$  (Figure 20b) there are three distinguishable vortices including the structure that is formed during the current cycle. For  $\phi = 180^\circ$  (Figure 20c) the data corresponds to ten 2000 Hz periods after the beginning of the cycle

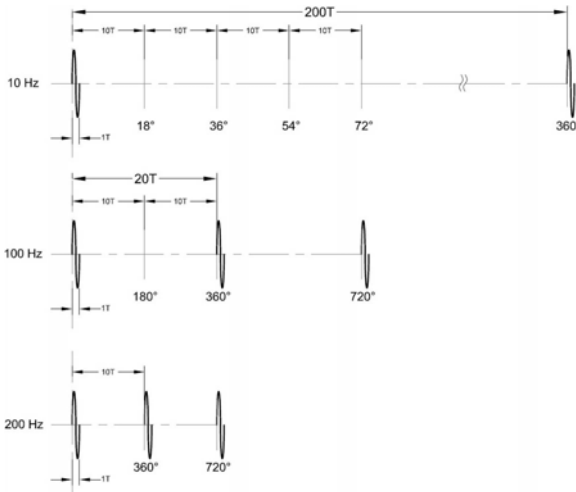


**Figure 21. Data acquisition timing for  $f_{AM} = 10 \text{ Hz}$ , 0.5% duty cycle,  $f_{AM} = 100 \text{ Hz}$ , 5% duty cycle, and  $f_{AM} = 200 \text{ Hz}$ , 10% duty cycle.**

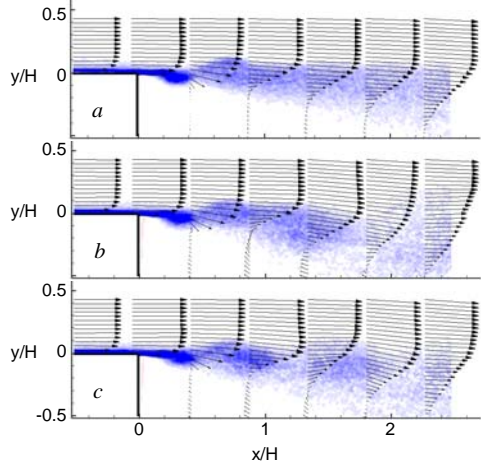
(which corresponds to Figure 20c) shows phase locked data at the half-point of the cycle and the structure formed in the previous cycle remains in the field of view at  $x/H = 1.3$ . Finally,  $f_{AM} = 200 \text{ Hz}$  is acquired (after ten 2000 Hz periods) at the end of the modulation cycle ( $\phi = 360^\circ$ , see Figure 21) and the shorter intervals allow vortices from three consecutive cycles to remain visible in figure 22c. It is interesting to note that the large scale structure (located at  $x/H = 0.3$ ) after ten periods remains a similar size for the three modulation frequencies in Figure 22 unlike the 50% duty cycle cases, which lead to different size structures at different modulation frequencies (see Figure 11).

The data in Figure 23 are acquired after twenty 2000 Hz actuation periods (10 ms) and are displayed for  $f_{AM} = 10 \text{ Hz}$ , 50 Hz, and 100 Hz with a schematic of the timing shown in Figure 21. The data for  $f_{AM} = 10 \text{ Hz}$  is acquired at  $\phi = 36^\circ$  (10% of the modulation cycle), the 50 Hz data at  $\phi = 180^\circ$ , and the 100 Hz case at  $\phi = 360^\circ$ . For the three

the final phase  $\phi = 72^\circ$  occurs after forty periods of the 2000 Hz actuation. The abrupt actuation creates a discontinuity in the vorticity field of the shear layer and a new CW vortex is induced. This discontinuity is located at  $x/H = 0.4$  in Figure 19a and becomes more visible at  $x/H = 1.2$  by  $\phi = 36^\circ$  (Figure 19b). Figure 19a corresponds to the partial field plot (Figure 18f) and the full field plot of Figure 19b coincides with Figure 18j. By the final phase after forty actuation cycles ( $\phi = 72^\circ$ , Figure 19d) the structure reaches  $x/H = 2$  and the vorticity distribution ( $-0.6 < x/H < 1$ ) appears very similar to the unforced flow. Since the coherent structures in shear layer move nominally at the average velocity of the two streams, the velocity of the structures here is expected to be approximately  $U_0/2$ , which means that the vortex in Figure 19 would be expected to move approximately  $x/H = 0.6 - 0.7$  between each of the phases. However, it is seen that it actually accelerates as it is advected without reaching  $U_0/2$  speed in the measurement domain. When a single pulse is formed using 100 Hz amplitude modulation with a 5% duty cycle (Figure 20), the shorter modulation period compresses the streamwise wavelength as shown in Figures 20a and 20b where the structures from the two previous cycles are visible in the measurement domain.

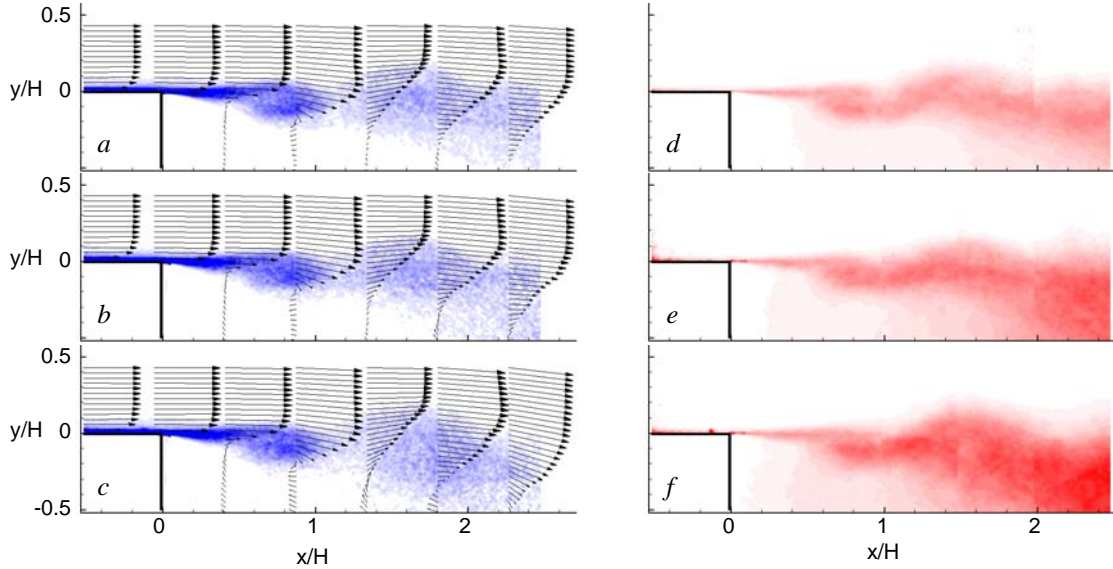
Ignoring the downstream differences, the data in Figures 18 and 19 appear similar in the range  $-0.6 < x/H < 0.4$ . Although the modulation period decreases, there is enough time to allow the shear layer vortex to evolve to a comparable size as for  $f_{AM} = 10 \text{ Hz}$ . The time increment between the phases in Figure 19 are five cycles of the 2000 Hz actuation indicating that the structure is expected to move approximately  $x/H = 1/3$  between each phase, whereas it is again seen that it actually accelerates during this time.

Figure 21 illustrates the relative timing schemes for various modulation cases, all with a single actuation vortex pair initiating each modulation cycle. The status of the flow after ten high frequency actuation periods is shown in Figure 22 for  $f_{AM} = 10 \text{ Hz}$ , 100 Hz, and 200 Hz. In all three cases the newly formed structure appears at  $x/H = 0.3$ . For  $f_{AM} = 10 \text{ Hz}$  in Figure 22a (which corresponds to Figures 18f and 19a) the data is acquired after 1/20 of the modulation cycle and only the single structure is visible. When  $f_{AM} = 100 \text{ Hz}$ , Figure 22b



**Figure 22.** Phase averaged (during 10 high-frequency actuation periods) vorticity concentrations at  $St_H = 7.36$  with:  $f_{AM} = 10$  Hz and 0.5% duty cycle (a),  $f_{AM} = 100$  Hz and 5% duty cycle (b), and  $f_{AM} = 200$  Hz and 10% duty cycle (c). Vorticity contour levels are the same as in Fig.6.

cases, the large structure has evolved to  $x/H = 0.8$  and in all cases it is equal size. For  $f_{AM} = 100$  Hz (Figure 23c) the structure from the previous modulation cycle is downstream of the current structure (see discussion of Figure 19). It is interesting to note that the vorticity plots (Figure 23i) for the three modulation frequencies are similar while the kinetic energy changes. For  $f_{AM} = 100$  Hz this structure from the previous modulation cycle [which can be seen in the vorticity distribution (Figure 23i-c) at  $x/H = 1.9$ ] is responsible for a significant increase in the turbulent kinetic energy in Figure 23f compared to 10 Hz and 50 Hz modulation in Figures 23d and 23e. The reason for increase in the kinetic energy for 50 Hz modulation (Figure 23e) compared to 10 Hz modulation (Figure 23d) is assumedly due to interaction with and feedback from the wall at  $y/H = 0$  which creates a reverse flow. It is speculated that for a free shear layer with no wall interaction there would be no discernable difference in the turbulent kinetic energy for the 10 Hz and 50 Hz modulation. This is supported by the virtually identical vorticity fields for the 10 Hz and 50 Hz modulation (Figures 23a and 23b).



**Figure 23.** Phase averaged (during 20 high-frequency actuation periods) vorticity (a-c) and turbulent kinetic energy (d-f) concentrations at  $St_H = 7.36$  with:  $f_{AM} = 10$  Hz and 0.5% duty cycle (a),  $f_{AM} = 50$  Hz and 2.5% duty cycle (b), and  $f_{AM} = 100$  Hz and 5% duty cycle (c). Vorticity contour levels are the same as in Fig.6 and TKE levels are the same as in Fig.10.

## VII. Conclusions

The concomitant small- and large-scale actuation of plane shear layers is investigated experimentally in a single-stream shear layer. The effects of the actuation are characterized spatially and spectrally by high-resolution PIV and hot wire measurements, respectively. The manipulation of the small-scale motions is directly induced by the high-frequency actuation nominally at frequencies that are an order of magnitude higher than the natural frequencies of the flow. While continuous, uninterrupted high-frequency actuation suppresses the formation of large coherent structures, large-scale motions (at scales comparable to the naturally-evolving vortices) are induced indirectly by transient startups of the high-frequency actuation. It is shown that these large structures are formed by a roll-up of

disrupted vorticity in the boundary layer at the point of separation, which entrains nearly stagnant fluid and thereby significantly impacts the shear layer spreading on the low speed side.

As was shown in earlier work, the train of high-frequency vortex pairs that issues into the boundary layer just upstream of separation results in suppression of turbulent kinetic energy by enhanced dissipation. Due to the cross flow (and boundary layer) dynamics, the CCW vortex in each pair is largely suppressed and accelerated around its CW counterpart and reaches the shear layer first. However, the major effect of the high-frequency actuation on the evolution of the shear layer occurs via interactions between the CW vortex train along the high-speed edge. The train of high-frequency vortices directly enhances energy at the small scales over an interaction region whose streamwise extent depends on the momentum coefficient of the actuation while suppressing the energy of the large scale motions. Spectral analysis shows that if the interaction region between the high-frequency vortices and shear layer is confined to the upstream boundary layer, turbulent kinetic energy is suppressed through most of the width of the shear layer except in a narrow domain along its low-speed edge. However, if the actuation level is sufficiently high so that the vortex train protrudes through the boundary layer and therefore interacts with the high-speed edge of the shear layer, the suppression of turbulent kinetic energy is confined to the center of the shear layer with two higher energy domains along the high- and low-speed sides. In that case, the suppression of the turbulent kinetic energy spreads towards the high-speed edge but is always bounded by the high entrainment zone on the low speed side.

When the high-frequency actuation is periodically started and stopped, each transient onset results in the formation of a large coherent structure along with a train of small-scale vortices. As they begin to interact, the faster advected high-frequency vortices coalesce either exclusively with the large structure formed during the same modulation period or also with the large structure formed during the previous modulation period. It is shown that the shear layer can simultaneously benefit from enhanced mixing through directly-induced the small-scale motions and enhanced entrainment via large-scale structures during concomitant excitation of both small and large scales. As a result, the turbulent kinetic energy is significantly enhanced and shear layer spreads faster.

Since the formation of a large coherent structure depends only on the transient disruption of the boundary layer vorticity, it is shown that a train of large coherent structures can be sustained simply by periodic pulsing of the shear layer at the desired rate using a single high-frequency actuation cycle.

### Acknowledgments

The present work has been supported in part by Air Force Research Laboratory and the Boeing Company.

### References

- <sup>1</sup>Brown, G. L. and Roshko, A., "On density effects and large structure in turbulent mixing layers," *J. Fluid Mech.*, Vol. 64, 1974, pp. 775–816.
- <sup>2</sup>Winant, C. D. and Browand, F. K., "Vortex pairing, the mechanism of turbulent mixing layer growth at moderate Reynolds number," *J. Fluid Mech.*, Vol. 63, 1974, pp. 237–255.
- <sup>3</sup>Wynagnanski, I. and Fiedler, H. E., "The two-dimensional mixing region," *J. Fluid Mech.*, Vol. 41, 1970, pp. 327–361.
- <sup>4</sup>Champagne, F. H., Pao, Y. H., and Wynagnanski, I. J., "On the two-dimensional mixing region," *J. Fluid Mech.*, Vol. 74, 1976, pp. 209–250.
- <sup>5</sup>Hussain, A. K. M. F. and Zaman, K. B. M. Q., "An experimental study of organized motions in the turbulent plane mixing layer," *J. Fluid Mech.*, Vol. 159, 1985, pp. 85–104.
- <sup>6</sup>Morris, S. C. and Foss, J. F., "Turbulent boundary layer to single-stream shear layer: the transition region," *J. Fluid Mech.*, Vol. 494, 2003, pp. 187–221.
- <sup>7</sup>Eaton, J. K. and Johnson, J. P., "A Review of Research on Subsonic Turbulent Flow Reattachment," *AIAA Journal*, Vol. 19, 1981, pp. 1093–1100.
- <sup>8</sup>Otugen, M. V., "Expansion ratio effects on the separated shear layer and reattachment downstream of a backward-facing step," *Exp. Fluids*, Vol. 10, 1991, pp. 273–280.
- <sup>9</sup>Nagib, H. M., Reisenthel, P. H., and Koga, D. J., "On the dynamical scaling of forced unsteady separated flows," *AIAA Paper* 85-0553, 1985.
- <sup>10</sup>Reisenthel, P. H., Nagib, H. M., and Koga, D. J., "Control of separated flows using forced unsteadiness," *AIAA Paper* 85-0556, 1985.
- <sup>11</sup>Kaiktsis, L. and Monkewitz, P. A., "Global destabilization of flow over a backward-facing step," *Phys. Fluids*, Vol. 15, 2003, pp. 3647–3658.
- <sup>12</sup>Chun, K. B. and Sung, H. J., "Control of turbulent separated flow over a backward-facing step by local forcing," *Exp. Fluids*, Vol. 21, 1996, pp. 417–426.
- <sup>13</sup>Chun, K. B., Lee, I., and Sung, H. J., "Effect of spanwise-varying local forcing on turbulent separated flow over a backward-facing step," *Exp. Fluids*, Vol. 26, 1999, pp. 437–440.

- <sup>14</sup>Vukasinovic, B., Lucas, D. G., and Glezer, A., "Direct manipulation of small-scale motions in a plane shear layer", *AIAA Paper* 2004-2617, 2004.
- <sup>15</sup>Mittal, R., Rampungoon, P., and Udaykumar, H. S., "Interaction of a Synthetic Jet with a Flat Plate Boundary Layer", *AIAA Paper* 2001-2773, 2001.
- <sup>16</sup>Park, S.-H., Lee, I., and Sung, H. J., "Effect of local forcing on a turbulent boundary layer", *Exp. Fluids*, Vol. 31, 2001, pp. 384–393.
- <sup>17</sup>Cui, J., Agarwal, R. K., and Cary, A. W., "Numerical Simulation of the Interaction of a Synthetic Jet with a Turbulent Boundary Layer", *AIAA Paper* 2003-3458, 2003.
- <sup>18</sup>Roberts, F.A. and Roshko, A., "Effects of Periodic Forcing on Mixing in Turbulent Shear Layers and Wakes", *AIAA Paper* 85-0570, 1985.
- <sup>19</sup>Oster, D. and Wygnanski, I., "The Forced Mixing Layer Between Parallel Streams", *J. Fluid Mech.*, Vol. 123, 1982, pp. 91-130.
- <sup>20</sup>Wiltse, J.M. and Glezer, A., "Manipulation of free shear flows using piezoelectric actuators", *J. Fluid Mech.*, Vol. 249, 1993, pp. 261-285.
- <sup>21</sup>Davis, S.A. and Glezer, A., "The Manipulation of Large- and Small-Scales in Coaxial Jets Using Synthetic Jet Actuators", *AIAA Paper* 2000-0403, 2000.
- <sup>22</sup>Smith, B.L. and Glezer, A. "Jet Vectoring using Synthetic Jets", *J. Fluid Mech.*, Vol. 458, 2002, pp. 1-34.
- <sup>23</sup>Ho, C-M. and Huang, L-S., "Subharmonics and Vortex Merging in Mixing Layers", *J. Fluid Mech.*, Vol. 119, 1982, pp. 443-473.